



HAL
open science

Investigating secondary ice production in a deep convective cloud with a 3D bin microphysics model: Part II - Effects on the cloud formation and development

Pierre Grzegorzcyk, Wolfram Wobrock, Antoine Canzi, Laurence Niquet,
Frédéric Tridon, Céline Planche

► To cite this version:

Pierre Grzegorzcyk, Wolfram Wobrock, Antoine Canzi, Laurence Niquet, Frédéric Tridon, et al..
Investigating secondary ice production in a deep convective cloud with a 3D bin microphysics model:
Part II - Effects on the cloud formation and development. *Atmospheric Research*, 2024, pp.107797.
10.1016/j.atmosres.2024.107797 . hal-04787194

HAL Id: hal-04787194

<https://hal.science/hal-04787194v1>

Submitted on 17 Nov 2024

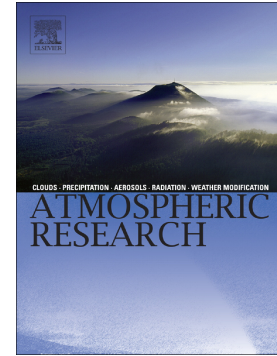
HAL is a multi-disciplinary open access archive for the deposit and dissemination of scientific research documents, whether they are published or not. The documents may come from teaching and research institutions in France or abroad, or from public or private research centers.

L'archive ouverte pluridisciplinaire **HAL**, est destinée au dépôt et à la diffusion de documents scientifiques de niveau recherche, publiés ou non, émanant des établissements d'enseignement et de recherche français ou étrangers, des laboratoires publics ou privés.

Journal Pre-proof

Investigating secondary ice production in a deep convective cloud with a 3D bin microphysics model: Part II - Effects on the cloud formation and development

Pierre Grzegorzcyk, Wolfram Wobrock, Antoine Canzi, Laurence Niquet, Frédéric Tridon, Céline Planche



PII: S0169-8095(24)00579-9

DOI: <https://doi.org/10.1016/j.atmosres.2024.107797>

Reference: ATMOS 107797

To appear in: *Atmospheric Research*

Received date: 26 July 2024

Revised date: 8 November 2024

Accepted date: 12 November 2024

Please cite this article as: P. Grzegorzcyk, W. Wobrock, A. Canzi, et al., Investigating secondary ice production in a deep convective cloud with a 3D bin microphysics model: Part II - Effects on the cloud formation and development, *Atmospheric Research* (2024), <https://doi.org/10.1016/j.atmosres.2024.107797>

This is a PDF file of an article that has undergone enhancements after acceptance, such as the addition of a cover page and metadata, and formatting for readability, but it is not yet the definitive version of record. This version will undergo additional copyediting, typesetting and review before it is published in its final form, but we are providing this version to give early visibility of the article. Please note that, during the production process, errors may be discovered which could affect the content, and all legal disclaimers that apply to the journal pertain.

Highlights

Investigating Secondary Ice Production in a Deep Convective Cloud with a 3D Bin

Microphysics Model: Part II - Effects on the cloud formation and development

Pierre Grzegorzczuk, Wolfram Wobrock, Antoine Canzi, Laurence Niquet, Frédéric Tridon, Céline

Planche

- Heterogeneous ice nucleation and fragmentation of freezing drops plays a role during formation of the cloud
- Hallett-Mossop and ice-ice breakup processes dominate after the cloud formation
- The impact of each SIP process on particle size distributions is analyzed by tracking air parcel trajectories
- SIP reduces precipitation amount
- SIP affects cloud dynamics
- Cloud top altitude is reduced due to SIP

Investigating Secondary Ice Production in a Deep Convective Cloud with
a 3D Bin Microphysics Model: Part II - Effects on the cloud formation
and development

Pierre Grzegorzcyk^{a,1}, Wolfram Wobrock^a, Antoine Canzi^a, Laurence Niquet^a, Frédéric Tridon^{b,a},
Céline Planche^{a,c,2},

^a*Universite Clermont Auvergne, CNRS INSU, Laboratoire de Meteorologie Physique UMR 6016,
F-63000, Clermont-Ferrand, France*

^b*Dipartimento di Ingegneria dell'Ambiente, del Territorio (DIATI), Politecnico di Torino, Turin,
Italy*

^c*Institut Universitaire de France (IUF), France*

*Email addresses: p.grzegorzcyk@opgc.fr (Pierre Grzegorzcyk), celine.planche@uca.fr (Céline
Planche)*

¹Corresponding author

²Corresponding author

Abstract

Secondary ice production (SIP) leads to the formation of new ice particles from preexisting ones. Besides generating ice crystals, SIP can also influence cloud characteristics, including convection, precipitation, and even radiative properties. This study examines the effect of ice crystal formation by Hallett-Mossop, fragmentation of freezing drops, and fragmentation due to ice–ice collision processes in an idealized deep convective cloud observed during the HAIC/HIWC campaign, using the 3D bin microphysics scheme DESCAM. Our results indicate that heterogeneous ice nucleation and fragmentation of freezing drops play a role during the early formation of the cloud while after that, Hallett-Mossop and ice-ice breakup processes dominate, representing 17.6% and 81.5% of the ice crystal production, for temperatures warmer than -30°C . For temperatures colder than -30°C , homogeneous and heterogeneous ice nucleation processes are the main contributors to ice crystal formation. The impact of each SIP process on particle size distributions is analyzed by tracking air parcel trajectories. This study also shows the effect of SIP processes on cloud development. Implementing SIP results in a decrease in cloud top altitude by around 1.5 km. Our analysis shows that this effect is caused by increased latent heat released below 11 km, resulting from a stronger vapor deposition on more numerous ice crystals. This enhances convection at lower levels but inhibits it above. Furthermore, incorporating SIP leads to 15% decrease in total precipitation amount and 25% reduction of intense rainfall (accumulated precipitation over 40 mm). Hence, our study emphasizes the importance of SIP mechanisms in cloud development and precipitation.

Keywords: Cloud microphysics, Convective cloud, Secondary ice production, Convection

1. Introduction

Our understanding of the processes and properties of the ice phase in clouds remains incomplete and raises numerous unresolved questions. One of them is the discrepancy between the number of ice nucleating particles (INPs) and observed ice crystal concentrations (N_{ice}), which has been documented for several decades. Multiple observational studies (e.g. Ladino et al., 2017; Järvinen et al., 2022; Korolev et al., 2022) and modeling investigations (e.g. Farrington et al., 2016; Fu et al., 2019; Kagkara et al., 2020) show that the effectiveness of primary ice production (PIP) processes (i.e. heterogeneous and homogeneous ice nucleation) alone cannot explain the observed ice crystals number concentrations (N_{ice}). This supports the existence of secondary ice production (SIP), which generates additional ice crystals from existing ones. The relevance of six of these processes observed in laboratory experiments was assessed by Korolev and Leisner (2020). However, based on current knowledge about SIP, only three of these processes are commonly discussed: the splintering during riming (hereafter called Hallett-Mossop) (Hallett and Mossop, 1974), fragmentation of freezing drops (hereafter called drop shattering) (Lauber et al., 2018; Keinert et al., 2020), and fragmentation due to ice-ice collision (hereafter called ice-ice breakup) (Vardiman, 1978; Takahashi et al., 1995; Grzegorzczuk et al., 2023).

Increased attention on SIP has emerged in recent years following studies such as Field et al. (2017) which highlights numerous uncertainties regarding these processes. Consequently, SIP has been intensively investigated through observations, including radar measurements (e.g. Billault-Roux et al., 2023; von Terzi et al., 2022) or by in situ measurements attempting to identify the processes responsible for ice crystal concentrations (e.g. Heymsfield and Willis, 2014; Korolev et al., 2020a; Brechner et al., 2023; Lawson et al., 2023).

Simultaneously, SIP processes have been implemented into models, showing both their

significant effectiveness and their various impacts at different scales. At regional scales, modeling studies of Sotiropoulou et al. (2021) and Zhao and Liu (2022) show that considering the SIP processes leads to supercooled liquid water contents in better agreement with observations in Arctic clouds, improving the partitioning between ice and liquid water phases. Therefore, regarding the influence of SIP on the radiative properties of clouds, Young et al. (2019) and Waman et al. (2022) demonstrated that considering SIP mechanisms leads to an increase in the amount of shortwave radiation. At a global scale, Zhao and Liu (2021) demonstrated that the effectiveness of the SIP processes depends on the cloud temperature and that SIP processes imply not only a decrease of the liquid water path but also an increase in the global annual average net cloud forcing ($+1.1 \text{ W m}^{-2}$). Other effects of the inclusion of SIP mechanisms have been observed such as changes in rain and snow precipitation (Hoarau et al., 2018; Dedekind et al., 2021; Georgakaki et al., 2022; Han et al., 2024) or even in convection intensity (Dedekind et al., 2021; Karalis et al., 2022; Qu et al., 2022).

SIP mechanisms result in newly formed ice crystals whose origin is not well understood. Indeed, SIP remains difficult to observe in real atmospheric conditions, and replicating SIP processes in laboratory experiments is challenging. A few laboratory studies are nevertheless available which allow the parameterization of SIP processes. However, these parameterizations are subject to various uncertainties.

The companion paper (Grzegorzczak et al., 2024, hereafter Part I) provides an assessment of different representations available in the literature for each of the three main SIP processes using the bin microphysics scheme DESCAM (DEtailed SCAvening and Microphysics model; Flossmann and Wobrock, 2010) applied in the same 3D dynamical frame. The main goal of Part I was to investigate how various parameterizations of secondary ice production (SIP) processes can

influence the microphysical properties such as ice crystal number concentration, particle size distributions, and both liquid and ice water contents of a deep convective cloud. Several representations for Hallett-Mossop (HM), fragmentation of freezing drops (DS), and ice-ice breakup (BRK) were tested. Our results were compared with in-situ observations to discuss the relevance of each SIP representation. The findings can be summarized as follows:

- Simulations without SIP underestimate the concentration of ice crystals at temperatures warmer than -30°C . In contrast, incorporating HM and BRK enhances the number of small ice crystals ($< 1\text{ mm}$) which improves the simulated particle size distributions compared to those observed by in situ observations. Regarding the concentration of ice crystals, SIP processes reduce discrepancies with observations by two orders of magnitude.
- Employing several parameterizations for DS reveals that DS minimally affects the properties of the cloud at its mature stage. This process may be efficient in the cloud development stage. However, for negative temperatures close to 0°C , where supercooled drops are most frequent, this process is not yet well characterized.
- All parameterizations of SIP processes exhibit the same trend: an increase in IWC and a decrease in supercooled LWC.
- The different parameterizations for the ice crystal sticking efficiency investigated significantly affect particle size distributions, ice crystal concentrations, and ice water content. Furthermore, the size of fragments generated by BRK significantly changes the shape of the ice particle size distribution.

In addition to Part I, which focused on numerical tests and comparisons with observations at the mature stage, this part II paper investigates the evolution of ice particle production by primary ice particle production (PIP) and secondary ice production (SIP), all along the evolution of

a deep convective cloud system. By using the detailed bin microphysics model DESCAM and online air parcel trajectories, we analyze the impacts of PIP and SIP on the evolution of ice particle size distributions. Furthermore, special attention is given to the influence of SIP on cloud dynamics by analyzing the cloud top altitude, vertical wind speed, and relative humidity, as well as their interactions with microphysical processes. Consequently, changes in precipitation due to SIP are also presented.

The paper is structured as follows: Section 2 provides a brief description of the simulation setup, including the parameterizations used here and already tested in Part I, as well as the methodology employed for analysis. Section 3.1 presents the results of the evolution of ice crystal production by PIP and SIP as well as their impact on particle size distribution. Section 3.2 is dedicated to the consequences of SIP on cloud convection and the possible reasons for these alterations. Finally, the effect of SIP on the amount of precipitation is presented in Section 3.3. A brief discussion comparing our findings with other studies is presented in Section 4. Conclusions and key points of this study are summarized in Section 5.

2. Model configuration and case specification

2.1. Model configuration

This study uses DESCAM bin microphysics scheme (DEtailed SCAvening and Microphysics model, Flossmann and Wobrock, 2010; Planche et al., 2010) which is implemented in the Clark-Hall non-hydrostatic and anelastic 3D dynamical model (Clark et al., 1996; Clark, 2003). DESCAM uses six distribution functions to describe aerosol particles, drops, ice crystals, rimed ice, as well as aerosol mass within each drop and each ice crystal bin. All the distributions are logarithmically spaced with mass doubling bins, which evolve freely. The warm (liquid phase)

microphysics processes represented in DESCAM are droplet nucleation and deactivation from the Köhler theory, vapor depositional growth, collision-coalescence and collisional breakup of drops. The represented cold (ice phase) microphysics processes are homogeneous ice nucleation following the approach of Monier et al. (2006) which was developed based on Koop et al. (2000), heterogeneous ice nucleation (deposition, condensation and immersion modes) from Hiron and Flossmann (2015), diffusional growth by vapor deposition, collisional processes such as riming and aggregation and finally secondary ice production (SIP) mechanisms: Hallett-Mossop, drop shattering and ice-ice breakup (more details in Grzegorzczak et al., 2024).

2.2. Case specification

The deep convective cloud case under study was observed in May 2015 during the HAIC-HIWC airborne campaign, which took place close to Cayenne in French Guyana (Fontaine et al., 2020; Hu et al., 2021). Simulations are conducted using a single domain of 354 grid points in x , 210 points in y , and 86 points in z , with 0.25 km horizontal resolution and 0.20 km vertical resolution. Simulations runs for 3 hours with a time step of 1 s. The initial atmospheric conditions are based on the sounding data from Macapa station observed on May 23, 2015, at 00:00 UTC. This sounding was modified by reducing wind speeds by a factor 1.3 below 10 km and 2 above, to ensure that the cloud remains within the domain. Aerosol number and size distribution are derived from UHSAS measurements provided in Ladino et al. (2017). The total number concentration of aerosol particles is set to 800 cm^{-3} at ground level and decreases exponentially to 100 cm^{-3} from 1.5 km altitude. The type of aerosol particle in DESCAM is assumed to be composed of NaCl, representing a marine origin.

To initiate convection, a circular thermal bubble of 8 km radius is applied during the first

25 minutes of the simulation and then progressively decreased with time (for more details, see Part D). The maximum latent and sensible heat fluxes of the perturbation are set to 1500 W m^{-2} (in the same range as Lasher-Trapp et al., 2018) while this intensity decreases horizontally (with a cosine function) and vertically (exponentially). A similar initiation method is used in Huang et al. (2022) for the same case. 3D data outputs are generated every 10 minutes, while profiles of averaged cloud properties and processes are available every 10 seconds.

In the companion paper, Grzegorzcyk et al. (2024), different SIP parameterizations recently available in the literature were evaluated using DESCAM by comparing simulated ice crystal number concentration (N_{ice}), ice water content (IWC), liquid water content (LWC) and particle size distributions (PSD) with HAIC-HIWC observations (based on 2D-S and PIP probes). As a result, the rate of fragments generated by the Hallet-Mossop is set here to 350 per mg of rime at -5°C based on Hallett and Mossop (1974). Although this value is commonly used in modeling studies, it is challenging to determine if it is more realistic than those from other laboratory experiments (e.g. Mossop, 1976; Heymsfield and Moosop, 1984). For the drop shattering mechanism, the parameterization of Phillips et al. (2018) is applied encompassing both mode 1 (drop collision with a less massive ice crystal or drop freezing) and mode 2 (drop collision with a more massive ice crystal). This parameterization seems to be the most reliable as it is based on several laboratory observations performed in the 1970-80's contrary to other approaches which are based on only a few studies. Finally, the ice-ice breakup process follows the approach of Phillips et al. (2017) but using parameters derived from laboratory experiments of Grzegorzcyk et al. (2023). The use of these specific parameterizations of the 3 SIP mechanisms considered in the study leads to a better agreement between simulated and observed mean N_{ice} . Fragments formed by the ice-ice collision breakup process are distributed into several bins based on the fragment size

distribution function detailed in Grzegorzczuk et al. (2023).

Name	Hallett-Mossop	Drop shattering	Ice-ice breakup
noSIP	-	-	-
HMonly	350 per mg	-	-
DSonly	-	Phillips et al. (2018)	-
BRKonly	-	-	Phillips et al. (2017) with Grzegorzczuk et al. (2023)
ALLSIP	350 per mg	Phillips et al. (2018)	Phillips et al. (2017) with Grzegorzczuk et al. (2023)

Table 1: Table of the different simulations performed with DESCAM model.

Two contrasted simulations will be done, one without any SIP processes (i.e. ice crystals formed only via homogeneous and heterogeneous ice nucleation) and another one with all the SIP processes included (i.e. Hallett-Mossop (HM), drop shattering (DS) and ice-ice breakup (BRK)). These numerical experiments are respectively called hereafter noSIP and ALLSIP (see Table 1). Furthermore, three additional numerical experiments are performed where only one SIP process is active (HMonly, DSonly or BRKonly) to study the individual influence of each process.

2.3. Parcel trajectories

To investigate the evolution of particle size distributions in DESCAM (see Section 3.1.2), we applied an online method to track the trajectories of individual air parcels. This consists of an ensemble of 100 initial points placed close to the 0 °C isotherm and horizontally dispersed in the

area where the cloud starts to develop. These trajectories follow the wind flow from cloud formation stage (40 min) up to the mature stage (80 min). All along these trajectories, the temperature, altitude, production rate of ice crystals by PIP and SIP mechanisms, as well as the ice crystal number concentration in each bin of the size distribution are recorded. Two of these trajectories are represented in 3.1.2.

3. Results

3.1. *The role of the primary and secondary ice production mechanisms*

This section is dedicated to the analysis of the dominant processes producing ice crystals along the evolution of the deep convective cloud investigated. First, the production rate of ice crystals is analyzed both vertically and horizontally from the formation stage (40 min) up to the mature stage of the cloud (80 min). Secondly, a special focus is put on the effect of PIP and SIP on particle size distributions.

3.1.1. *Spatio-temporal evolution of production rates of primary and secondary ice formation processes*

Fig. 1a,b and c show vertical cross-sections of the ice crystal production rate for the ALLSIP simulation, focusing on the initial generation of ice crystals and the onset of cloud glaciation. Fig. 1d,e and f present horizontal cross-sections of the ice crystal production at 6 km (-7°C) for the same moments. At this temperature level, all three SIP processes can be active, indicating which process is dominant depending on the cloud lifetime.

In these figures, each pie chart represents the spatial averaged ice crystals production rate (with a radius in logarithmic scale) for PIP and SIP processes. In contrast to Fig. 1 which focuses

on ice initiation, Fig. 2 is dedicated to the evolution of the cloud up to its mature stage. It shows the horizontally averaged PIP and SIP rates (for $RH_{ice} > 100\%$) as a function of time and altitude. This illustration is similar to Fig. 8 of Huang et al. (2022) for the same simulation case.

Figure 1: Vertical cross sections (a,b,c) of production rate of SIP and PIP during the cloud formation along a plane that intersects the convective core of the cloud. Panels (d, e, f) present horizontal cross sections at 6 km altitude (-7°C). Pie charts depict the contribution of each process in the ALLSIP experiment (averaged of 4×4 grid points) as well as the total magnitude of ice number production from the radius of the pie which changes logarithmically.

Figure 2: Temporal evolution of the mean horizontal ice crystal production rate for SIP and primary ice production mechanisms for cloudy points where $RH_{ice} \geq 100\%$ from the ALLSIP experiment. Pie charts depict the contribution of each process as well as the total magnitude of ice number production from the radius of the pie which changes logarithmically. The two parcel trajectories analyzed in section 3.1.2 are represented by full (traj 1) and dotted lines (traj 2).

Fig. 1a shows that at 6 km altitude (i.e. -7°C), ice crystals are initially formed via heterogeneous ice nucleation at a rate of around $5 \times 10^{-5} \text{ cm}^{-3} \text{ s}^{-1}$. During the ascent of the forming cloud, heterogeneous ice nucleation triggers the formation of ice crystals at the top of the ascending parcel (Fig. 1b). At 6 km altitude (Fig. 1d), heterogeneous ice nucleation only dominates the production of ice crystals for about 2 minutes and becomes thereafter less important due to the dominant secondary ice production for $T > -30^\circ\text{C}$. Still at this altitude but 2 min later (Fig. 1f), heterogeneous ice nucleation only plays a role when the cloud starts to extent

horizontally, forming ice crystals on the cloud edges. At higher altitudes (> 12 km), as depicted in Fig. 2, heterogeneous and homogeneous ice nucleation processes form ice crystals in the cloud anvil at $T < -30^{\circ}\text{C}$ with much stronger rate (more than $10^{-2} \text{ cm}^{-3} \text{ s}^{-1}$). However, after 70 min both PIP processes cease to generate a substantial quantity of ice crystals.

Fig. 1b and Fig. 1e show that DS becomes dominant just after the crystals have been generated by heterogeneous ice nucleation. At this stage, the cloud is mainly liquid and large supercooled drops are advected by the strong updrafts. Fig. 1b especially shows the ascending parcel in which ice crystals are generated by heterogeneous ice nucleation at the cloud top (7 km) while DS dominates below with a rate up to $10^{-3} \text{ cm}^{-3} \text{ s}^{-1}$. Our results indicate that DS mode 2 is stronger than DS mode 1 which is only efficient close to -10°C but never dominates the production of ice crystal. The time span with dominating DS lasts less than 5 minutes during the early glaciation of the cloud, which is coherent with observations of Lawson et al. (2015), who demonstrated that the glaciation of an ascending cloud is rapid and coincides with the presence of large frozen/broken drops. After 40 min, as illustrated in Fig. 2, DS only produces a significant part of ice crystals next to 0°C altitude (around $10^{-4} \text{ cm}^{-3} \text{ s}^{-1}$) via the mode 2 (see Phillips et al., 2018) where large drops can collide with more massive ice crystals. It should be noted that BRK is triggered around -15°C in Fig. 1b and quickly becomes stronger than DS via mode 1, which is only slightly visible at 7 km in Fig. 2. This explains why DS via mode 2 only dominates near the melting layer, where no other SIP processes are active. The fact that mode 2 is the dominant mode of DS is similar to conclusions of James et al. (2023).

As shown by the transition from Fig. 1e to Fig. 1f, HM becomes efficient after DS, when the cloud starts to glaciate. Indeed, the presence of large ice surfaces is necessary for riming and triggering the HM process which becomes rapidly more efficient than DS. Therefore, as illustrated

in Fig. 2, HM is efficient between 6 and 9 km before 45 min of simulation with a rate of approximately $10^{-3} \text{ cm}^{-3} \text{ s}^{-1}$. Later in the simulation, the HM process continues to dominate the production of ice crystals at a similar rate but in a restricted zone close to 6 km altitude (-7°C). This contrasts to BRK, which dominates from 7 to 12 km. However, the local production of ice crystals by HM increases N_{ice} on a wide vertical range, up to levels at -20°C by vertical transport (Grzegorzczak et al., 2024).

The ice-ice breakup process exerts the strongest vertical influence, dominating the production of ice crystals between 7 and 12 km altitude after 45 minutes, with a rate of around $10^{-3} \text{ cm}^{-3} \text{ s}^{-1}$ below -30°C (see Fig. 2). It becomes efficient after the formation of large ice crystals, similar to HM (see Fig 1). Contrary to other SIP processes, BRK does not necessitate supercooled liquid drops but only large and fragile ice crystals that collide and produce fragments (see parameters in Phillips et al., 2017). As obvious from vertical profiles in Fig. 3, supercooled liquid water content is low above 7 km when the cloud reaches its mature stage (80 min), which may explain why BRK is efficient at longer stages, up to 12 km (i.e. -45°C). However, this mechanism can be limited by ice crystal sedimentation or by decrease in updrafts which restricts the number of large ice crystals. The presence of secondary ice crystals was reported at low temperatures (between -22°C and -27°C) in Korolev et al. (2022) associated with the presence of large ice crystals as well as rimed particles covered by ice crystals formed by deposition growth. As presented in Grzegorzczak et al. (2023) vapor grown crystals on rimed particle produce a large amount of fragments during collisions. Furthermore, as presented in Fig 2, BRK occurs at such temperatures, which suggests BRK as a plausible candidate for the production of ice crystals at low temperatures.

Figure 3: Vertical profile of mean ice water content (IWC) in solid lines and liquid water content (LWC) in dashed lines for noSIP and ALLSIP simulations at the formation stage (50 min) in (a) and beginning of the mature stage (80 min) in (b). Only data points with total water contents (TWC) greater than 0.01 g m^{-3} are taken into account.

A strong effect of homogeneous ice nucleation above 10 km ($T < -30^\circ\text{C}$) is visible during the cloud development phase, 10 minutes after the formation of the first ice crystals (see Fig 2). Homogeneous ice nucleation is dependant on ice supersaturation which is high at the top of the ascending air parcel during the cloud formation as presented in Fig. 1c and f. Furthermore, this process is also active next to the cloud top (i.e. 15 km) during the formation of the anvil simultaneously to heterogeneous ice nucleation. However, after 70 minutes when the anvil is formed, ice supersaturation decreases next to the cloud top which reduces the production of ice crystals by this mechanism.

Throughout the entire cloud lifetime, in regions where $T < -30^\circ\text{C}$, over 99 % of ice crystals are formed through PIP, indicating that SIP is negligible at low temperature. In contrast, for $T > -30^\circ\text{C}$, 81.5 % of ice crystals are generated by BRK and 17.6 % by HM, which are the dominant processes for ice crystal production. In this temperature range, only 1.4 % of ice crystals are produced by DS and only 0.2 % by PIP which are both playing significant role only during cloud glaciation.

3.1.2. *Effect of PIP and SIP on particle size distributions*

Some attempts have been made to identify the processes influencing the PSD characteristics from in situ measurements (e.g. Heymsfield and Willis, 2014; Korolev et al.,

2020a; Brechner et al., 2023; Lawson et al., 2023). However, characterizing the production mechanisms of ice crystals from such measurements remains challenging. Furthermore, little attention has been made by modeling studies on the size of ice crystals generated by secondary or primary ice processes as well as their evolution across the particle size distributions (PSDs).

From the ensemble of trajectories, two were selected, as illustrated in Fig. 2 by solid and dashed black lines. These two trajectories were chosen as in at least one of their part, a single process dominates the production of ice crystals, illustrating the effect of a single PIP or SIP on ice PSDs. They referred to Traj 1 and Traj 2, start at 40 minutes and at altitudes of 4 km and 4.5 km respectively (see Fig 2).

The trajectories follow the airflow and therefore do not track individual falling ice crystals. However, since the focus is on the small ice crystals formed by SIP that fall slowly, the impact of sedimentation on PSDs is considered negligible over the short periods depicted in Fig. 4. It is also important to note that these trajectories are provided as examples to investigate the impact of the different PIP and SIP processes on PSD throughout the cloud evolution, and are not representative of the overall cloud evolution which is depicted in Fig. 2.

The analyses of these trajectories show the influence of the different ice formation processes on the evolution of the PSD during the formation of the cloud. Fig. 4a-c illustrate the effect of HM, BRK and heterogeneous ice nucleation mechanisms on the PSDs along Traj 1 while Fig. 4d shows the same analysis for homogeneous ice nucleation along Traj 2. In all panels of Fig. 4, the instantaneous vertical wind speed, LWC, IWC, N_{ice} , RH, altitude, and temperature are plotted to show the cloudy conditions belonging to the PSD represented in solid lines.

Figure 4: Particle size distribution of ice crystals from the ALLSIP experiment at various times

affected by Hallett-Mossop (a), ice-ice breakup (b) and heterogeneous ice nucleation (c) processes along Traj 1 while Traj 2 illustrates the effect of homogeneous ice nucleation (d). The vertical wind speed, LWC, IWC, N_{ice} , RH, altitude and temperature indicated on each panel represent the cloudy conditions associated with the PSD in solid colored lines.

For Traj 1 in Fig. 4a, at 40.01 min, the modeled PSD at 5.4 km is quite irregular and $N_{ice} = 0.004 \text{ L}^{-1}$. Only 15 seconds later, the air parcel reaches 5.6 km (-3.5°C) (see PSD in red in Fig 4a). During this brief ascent, the riming process becomes active, resulting in a decrease in LWC from 0.8 g m^{-3} to 0.5 g m^{-3} . The presence of riming with a temperature close to -3.5°C is favorable to trigger the Hallett-Mossop process. Indeed, at 40.25 min, a distinct new mode appears next to $15 \mu\text{m}$ as a result of HM effectiveness. Furthermore, the presence of riming is also characterized by the increase in the concentration of large ice crystals ($> 500 \mu\text{m}$) visible from 40.25 to 40.75 min.

In DESCAM model, fragments from the HM process are sized according to Choulaton et al. (1978, 1980), where fragments of around $10 \mu\text{m}$ were observed (see Grzegorzczuk et al., 2024, for details). Consequently, as depicted in Fig. 4a, small fragments generated by HM can grow rapidly by vapor deposition, from a size of $15 \mu\text{m}$ up to $40 \mu\text{m}$ in 30 seconds and form a mode close to $100 \mu\text{m}$ after 90 seconds. This confirms that looking at newly grown small ice crystals, as proposed by Korolev et al. (2020a), can be a method to detect the secondary ice production by HM using in-situ probes. Moreover, Fig. 4a shows that fragments may be faster than estimated by Heymsfield and Willis (2014). They suggest that columns or hexagonal plates originating from fragments of $10 \mu\text{m}$ size could be observed after approximately 150 to 300 seconds of growth. The faster growth suggested here could be due to the presence of high humidity ($\text{RH} = 102.26\%$).

Along Traj 1, DS is not a predominating process according to the analysis of the evolution

of the PSDs. However, it should be noted that since DS produces fragments of similar sizes to those from the HM process, distinction of these two processes from observations at $T < -8^{\circ}\text{C}$ may be challenging. At lower temperatures, DS could become distinguishable and would induce similar changes in PSD as HM.

Then, the air parcel of Traj 1 reaches 7.4 km (i.e. -14.4°C) at 41.75 min. Between 41.75 and 43.33 minutes (Fig. 4b), BRK process becomes dominant, increasing the ice crystal concentration from 140 L^{-1} to 540 L^{-1} in less than 2 minutes. The ice fragments generated by BRK in DESCAM predominantly consist of hundred micrometers size ice crystals based on Grzegorzczuk et al. (2023) observations, which lead to an increase in N_{ice} within the size range of $30\text{ }\mu\text{m}$ to 3 mm , with the most significant increase occurring close to $150\text{ }\mu\text{m}$. Consequently, as fragments have sizes close to the prevailing mode of the PSD, a new secondary mode is not visible (see Fig. 4b). This confirms the suggestion made by Korolev et al. (2020a) that fragments produced by BRK may not grow in the shape of small faceted ice crystals, thus making their identification during in situ measurements difficult. Furthermore, these fragments can be pieces of ice crystals having a distinct morphology (e.g. branches of dendrites) which can also be attributed to the shattering effect of in situ probes. Note that due to strong supersaturation and the rise in N_{ice} , the depositional growth increases the IWC from 1.82 to 3.54 g m^{-3} as depicted by the shift of the PSD to larger sizes (Fig. 4b). The presence of large ice crystals facilitates the BRK process, as they possess substantial fall speeds, resulting in high collision kinetic energy (CKE). Large ice crystals have large surface area, enabling fragmentation of numerous asperities. Both of these conditions are taken into account for this process when using the parameterization of Phillips et al. (2017). The presence of large ice crystals was not encountered at the start of Traj 1 which might explain why HM initially dominates the production of ice crystals at -3.5°C (see Fig. 4b). Furthermore, based

on Takahashi et al. (1995), the BRK process is parameterized to be less efficient in DESCAM at such temperatures compared to -15°C .

At 43.33 min, Traj 1 reaches 10 km altitude and temperatures lower than -30°C (see full line of Fig. 2). At this altitude, the parcel is not only influenced by BRK but also by heterogeneous ice nucleation. The decrease in temperature down to -30°C as well as the presence of high relative humidity ($\text{RH} = 78\%$ in Fig. 4c) cause that PIP processes dominate the production of ice crystals, increasing N_{ice} close to 1000 L^{-1} . This production of ice crystals from interstitial aerosol and remaining droplets is characterized by a second mode of small ice crystals around $20 \mu\text{m}$, which is illustrated by the green line at 44 min in Fig. 4c.

Traj 2 (see dashed line in Fig. 2) starts in a higher altitude compared to Traj 1 and reaches lower temperatures, where homogeneous ice nucleation becomes important. A short section of Traj 2 is represented in Fig. 4d, where N_{ice} increases from 340 L^{-1} to around 1200 L^{-1} in only one minute. Indeed, homogeneous ice nucleation is triggered by low temperatures (-37.9°C here) as well as the presence of high humidity ($\text{RH} = 97\%$) which is a consequence of strong vertical wind speeds encountered during the formation stage of the cloud (before 80 min). The effect of both heterogeneous and homogeneous ice nucleation occurs under similar conditions and lead to similar changes in PSD i.e. the creation of a mode of small ice crystals as depicted in Fig. 4c and Fig. 4d.

3.2. *Effects and mechanisms induced by secondary ice production on the cloud development*

3.2.1. *Effect of SIP on cloud dynamics*

Fig. 5 shows the temporal evolution of the mean cloud top altitude for the simulations

mentioned in Table. 1. The cloud top altitude is defined here as the mean of the maximum altitude where $TWC > 0.01 \text{ g m}^{-3}$ occurs. Fig. 5 indicates that considering SIP processes (individual or all SIP processes) leads to a noticeable decrease of cloud top altitude, starting from cloud formation at 50 min, persisting through its mature (from 80 min) and dissipation stages (from 120 min). The DOnly and HOnly simulations both show a reduction in cloud top altitude of about 1 km, whereas BRKOnly and ALLSIP gives a decrease by 2 km and 1.5 km. However, it remains difficult to explain why BRKOnly gives a lower cloud top altitude compared to ALLSIP. Nevertheless, this indicates that BRK process is the SIP mechanism that most significantly influences the cloud top altitude, possibly due to its dominance across the cloud vertical extent as illustrated in Fig. 2. Our results are in agreement with Karalis et al. (2022) who observed a lower cloud top as a consequence of BRK contrary to Qu et al. (2022) who found that the cloud tops are higher when including DS process.

Figure 5: Temporal evolution of the mean cloud top altitude for noSIP, individual SIP (HOnly, DOnly BRKOnly) and ALLSIP simulations described in Table. 1.

The altitude of the cloud top could be influenced by the vertical wind, as examined by Fig. 6 which displays the vertical occurrences of updrafts between $+1$ and $+2.5 \text{ m s}^{-1}$ as well as downdrafts between -2.5 and -1 m s^{-1} inside the cloud (where $TWC > 0.01 \text{ g m}^{-3}$) integrated over the entire cloud lifetime (up to 180 min). These ranges of vertical wind speeds were chosen as they correspond to the typical vertical wind speeds observed during the flights of the HAIC/HIWC campaign. Fig. 6 shows that the occurrence of updrafts and downdrafts decreases by a factor of 2 above 13 km, when considering any SIP or all SIP mechanisms compared to noSIP. This

diminution next to the cloud top may explain the lower cloud top obtained with SIP in Fig. 5.

Figure 6: Vertical occurrence of updrafts of $w = [1,2.5] \text{ m s}^{-1}$ in (a) and downdrafts of $w = [-2.5,-1] \text{ m s}^{-1}$ in (b) integrated over time and horizontal extension of the cloud for $\text{TWC} > 0.01 \text{ g m}^{-3}$.

Fig. 6a shows a rise of updraft occurrences in HMonly next to 7 km and 10 km. For BRKonly, there is a more pronounced increase in updraft occurrences between 9-12 km. These changes are consistent with the fact that the HM mechanism operates at lower altitudes compared to BRK (see Fig. 2). The occurrence of updrafts is stronger at 10 km in ALLSIP. The reasons for these changes are presented in Section 3.2.2.

Occurrences of downdrafts (Fig. 6b) are significantly higher between 8 and 11 km for HMonly, BRKonly and ALLSIP where the occurrence is doubled compared to noSIP. Contrary to the other experiments, DOnly leads to a slight decrease in downdraft occurrences between 8 and 11 km. Overall, both panels of Fig. 6 indicate that HMonly, BRKonly and ALLSIP give an intensified dynamics within the cloud (between 7-11 km) while it decreases at higher levels of the cloud (above 11 km) in comparison to noSIP. We suppose that the significant increase of downdrafts for ALLSIP simulation might result as a balancing effect triggered by the strong updraft occurrences in the same case.

3.2.2. SIP-induced mechanisms altering convection

The inclusion of SIP mechanisms leads to higher ice crystals concentrations (two orders of magnitude at -10°C as shown in the companion paper, Grzegorzczuk et al., 2024), leading to a faster

and more pronounced glaciation. As illustrated in Fig. 3a and b, ALLSIP produces higher IWC and lower supercooled LWC during both the formation stage (50 min) and the mature stage (80 min). The rise in IWC found in Fig. 3a,b could be linked to the changes in convective properties within the cloud (Fig. 5 and Fig. 6). To investigate these differences, Fig. 7 shows the temporal evolution of the mean vertical profile of difference in latent heat release between ALLSIP and noSIP. Positive values (in red) indicate a higher latent heat release due to SIP mechanisms, while negative values (in blue) indicate a lower latent heat release in the presence of SIP mechanisms. Note that data used for latent heat are mean values for all the cloudy grid points in a given altitude. It must be pointed out that all mean values of latent heat (for noSIP and ALLSIP) are positive until the dissipation stage at 120 min. This, does not exclude that presence of regions where RH_{ice} is well below 100% and sublimation can take place.

Figure 7: Temporal evolution of the changes in mean latent heat released between ALLSIP and noSIP simulation as function of altitude. Red area indicates a higher latent heat release for ALLSIP, while blue indicates a lower release. Only grid points with $TWC > 0.01 \text{ g m}^{-3}$ are taken into account.

As presented in Fig. 7, a clear surge in latent heat release is obtained before 70 min and below 10 km. Note that the maximum latent heat released at this stage reaches up to $0.035 \text{ }^\circ\text{C s}^{-1}$ (not illustrated). The surge of heat released corresponds to the region where SIP mechanisms generate ice crystals in an amount exceeding several orders of magnitude of those produced by PIP processes (see Fig. 6 of Grzegorzczak et al., 2024). Small fragments formed by SIP processes grow by vapor deposition to quickly reach bigger sizes (as illustrated in Fig. 4).

Figure 8a and b compare the rates of vapor deposition, riming, and drop condensation (i.e., variations in IWC or LWC). During the cloud formation stage (50 min), vapor deposition as well as riming rates increase and are shifted at lower altitudes due to SIP. The increase in ice crystal concentration caused by SIP probably enhances riming with more frequent ice-drop collisions and intensifies vapor deposition by depleting water vapor faster. Although the rate of riming is stronger than the rate of vapor deposition in Fig 8a, the latent heat released due to vapor deposition is significantly higher than that of riming. Indeed, at 50 min and 7.5 km, vapor deposition gives $4 \times 10^{-3} \text{ }^\circ\text{C s}^{-1}$ compared to $1 \times 10^{-4} \text{ }^\circ\text{C s}^{-1}$ for riming. Regarding Fig. 7, vapor deposition is the major contributor for the increase in latent heat, representing around 70 % of the total rise. Riming significantly contributes to latent heat rise below 6.5 km altitude and accounts for about 15% in overall increase.

Figure 8: Mean vertical profiles of condensed mass changes due to vapor deposition, riming and drop condensation for ALLSIP and noSIP simulations for the cloud formation stage (50 min) in a) and start of the mature stage (80 min) in b). Only grid points with $\text{TWC} > 0.01 \text{ g m}^{-3}$ are taken into account.

Conjointly to the analysis of latent heat release, Fig. 9 shows vertical median profiles of relative humidity with respect to ice (RH_{ice}) at 50 min (initiation stage) and 80 min (mature stage) for the noSIP and ALLSIP simulations. The left limit of the shaded region represents the 1st quartile, while the right limit represents the 3rd quartile for ALLSIP (green) and noSIP (grey). Fig. 9a illustrates that the water vapor is consumed as the cloud develops vertically, leading to a decrease in the 3rd quartile of RH_{ice} from 125% in noSIP to 110% in ALLSIP at 8 km. This

reduction is consistent with the observed rise in latent heat release shown in Fig. 7 as well as the rise in vapor deposition in Fig. 8a. Above 10 km, the lower amount of latent heat released in ALLSIP simulation during the cloud formation (before 80 min) could be due to the anterior consumption of water vapor at lower altitudes. This effect is visible in Fig. 8a with the shift of vapor deposition at lower altitudes. Consequently, in ALLSIP, the cloud buoyancy strengthens at lower altitudes while it weakens above 10 km (see black and green solid lines in Fig. 6a). Water vapor depletion due to secondary ice production was reported in several other studies, especially when BRK process was included (Hoarau et al., 2018; Dedekind et al., 2021).

Figure 9: Mean vertical profiles of relative humidity with respect to ice ($TWC > 0.01 \text{ g m}^{-3}$) for ALLSIP and noSIP simulations for the cloud formation stage (50 min) in a) and start of the mature stage (80 min) in b). Solid lines represent the median RH_{ice} and the limits of colored area correspond to the 1st and 3rd quartiles.

After 60 min and above the melting layer (4.5 km), the latent heat release becomes weaker for ALLSIP (see Fig. 7). First, water vapor is more rapidly depleted during cloud formation in ALLSIP, which might take longer in the noSIP simulation. Indeed, it may occur later in noSIP due to the lower number of crystals present below 10 km (e.g. 1 L^{-1} in noSIP instead of 50 L^{-1} for ALLSIP at 6 km and 100 min). Secondly, as shown in Fig. 9b, the first quartile of RH_{ice} becomes higher for ALLSIP ($RH_{ice} = 75\%$) than for noSIP ($RH_{ice} = 50\%$), which is not the case during the formation of the cloud at 50 min (Fig. 9a). We suppose that this increase is due to the stronger sublimation of ice crystals which is triggered by the rise of N_{ice} generated by SIP. The presence of this zone of sublimation at 80 min is also visible in Fig. 8b where vapor deposition becomes

negative. Additionally, the significant reduction in latent heat release (see Fig. 7) above 5 km after 60 minutes further confirms the development of areas dominated by sublimation. This conclusion is coherent with our finding for downdrafts whose occurrence is higher at altitudes from 5 to 11 km for the ALLSIP case (Fig. 6b). Relative humidity in downdrafts of cloudy air parcels decreases rapidly below saturation and causes sublimation.

Furthermore, it is also visible from Fig. 7 that the amount of latent heat released is higher under the melting layer (4.5 km) from 45 min to 100 min in ALLSIP. This phenomenon could be due to the presence of more numerous droplets (not shown here) caused by melting of small ice crystals originally produced by SIP processes. More numerous drops may increase the consumption of water vapor, as supported by the rise of vapor condensation at $T > 0$ °C in Fig. 8a and b. This therefore causes a stronger release of latent heat in a similar way as inside the ice phase. However, this phenomenon happens delayed (up to 100 min) since ice crystals are generated above 4.5 km by SIP and slowly precipitate.

3.3. *Impact of SIP on surface precipitation*

As depicted previously, SIP can affect the development of convective cloud systems, suggesting that it could also impact precipitation. In this context, Table. 2 illustrates the total amount of rainfall and the intense amount of rainfall (> 40 mm) in megatons obtained for each simulation at 180 min. Both rainfall amounts decrease when considering one or several SIP processes. The SIP mechanism that most significantly impacts precipitation is BRK, with a reduction in the total rainfall amount by approximately 8% and a decrease of the total amount of intense precipitation (> 40 mm) by 15% compared to noSIP. ALLSIP simulation results in a similar total precipitation amount as BRK but causes the greatest reduction in intense rainfall of

25% compared to noSIP. Although the variation of these two quantities appears to be only slightly affected, even small variations in rainfall amounts represent changes of megatons of precipitated water.

Rainfall amount (Mt)	noSIP	HMonly	DSonly	BRKonly	ALLSIP
Total	2.38	2.34	2.35	2.20	2.21
> 40 mm	0.62	0.51	0.60	0.53	0.47

Table 2: Total and > 40 mm rainfall amount (in megaton) accumulated up to 180 min for noSIP, HMonly, DSonly, BRKonly and ALLSIP simulations.

Going back to Fig. 3 we can see an increase in IWC while LWC (especially the concentration of large raindrops, not illustrated) is decreasing. Additionally, below the melting layer, droplet concentration rises due to the melting of small ice crystals generated by SIP, leading to stronger drop condensation and latent heat release (see Fig. 7 and Fig. 8). This increase in droplet number and decrease in raindrop concentration may reduce sedimentation as well as the efficiency of the collision-coalescence process, further lowering precipitation. A similar effect occurs when increasing aerosol number concentration (i.e. CCN), resulting in more droplets and less rainfall, as presented in Leroy et al. (2006), Leroy et al. (2009), Planche et al. (2010), and Kagkara et al. (2020).

It should be noted that incorporating a single SIP process reduces the total rainfall amount in our results. However, combining all SIP processes in the ALLSIP simulation results in a greater total rainfall amount compared to BRKonly. Similarly, the BRKonly simulation shows a more pronounced diminution of the cloud top altitude compared to ALLSIP (see Fig. 5). The different behavior of the ALLSIP simulation compared to BRKonly may arise from interactions and

feedback between SIP processes that influence cloud development. However, understanding these interactions remains challenging to understand and requires further investigation.

4. Discussion

Investigations on the role of SIP mechanisms in convective clouds by modeling studies led until today to quite different results. Several studies indicate that BRK dominates the production of ice crystals in deep convective clouds (Qu et al., 2020; Huang et al., 2022; Waman et al., 2022; Han et al., 2024). However, these studies depict different contributions of HM and DS processes. In our study, we found that DS is effective only during cloud formation, whereas HM contributes significantly during longer stages, representing 17.5% of ice crystals produced at temperatures warmer than -30°C (see Fig. 2). In Qu et al. (2020), HM is found to be negligible and DS is highly efficient during the cloud glaciation. Conversely, Waman et al. (2022) supports the significance of HM during the cloud formation while DS remains low. At the cloud mature stage, Huang et al. (2022) reports a stronger effect of DS compared to HM. Other studies such as Qu et al. (2022) include exclusively DS and found that it strongly enhances N_{ice} at the cloud mature stage. All of these results might differ as different microphysics schemes and numerical methods are employed. However, Huang et al. (2022) used similar parameterization compared to our study (i.e. Phillips et al., 2018 for DS and Hallett and Mossop, 1974 for HM) but we found in our study a stronger effect of HM and a weaker one for DS. These different results could be due to the different representations of the liquid phase mechanisms as droplet activation, growth by vapor deposition or collision coalescence which are treated in a detailed way in DESCAM (e.g. solving the stochastic equation) and therefore differ from the P3 scheme (Morrison and Milbrandt, 2015) of WRF used in Huang et al. (2022). The parameterization of drop coalescence and breakup are

sparse (Niquet et al., 2024) and can lead to major differences in terms of number of large and small droplets (as discussed in Tridon et al., 2019; Planche et al., 2019) which strongly impact the efficiency of both HM and DS processes.

The impact of the different SIP process may depend on cloud types and environmental conditions. However, given the substantial differences in the conclusions regarding SIP dominance for specific cloud types, such as convective clouds presented previously, identifying a clear trend in SIP dominance remains challenging. However, studies investigating SIP for different cloud types by using a single model could address this issue.

Instead of applying cloud modeling, Brechner et al. (2023) investigated the ice crystal production mechanisms based on in-situ measurements of the PSD as observed in convective clouds during the HAIC/HIWC campaign in Darwin 2014. Clouds investigated were similar to those observed during the HAIC/HIWC Cayenne campaign. Brechner et al. (2023) conclude that the presence of a small mode next to 50 μm diameter in bimodal or trimodal PSDs can be attributed to PIP mechanisms. This, is not supported by our results (see Fig. 4c and d) as the appearance of small mode due to PIP mechanisms only occurs for low temperatures ($T < -30^\circ\text{C}$), during the formation stage of the cloud i.e., before 80 min. Furthermore, Fig. 2 confirms that PIP processes globally dominate the production of ice crystals only for $T < -30^\circ\text{C}$ up to the cloud mature stage (80 min). For warmer temperatures ($T > -30^\circ\text{C}$), our results indicate that the presence of a mode of small ice crystals next to 20 μm could be due to effective HM or DS processes. Furthermore, the analysis of Traj 1 in section 3.1.2 shows that small ice particles of 10 μm produced by HM grow very quickly by vapor diffusion to larger sizes of 100 μm in a region of strong vertical transport as illustrated in Fig. 4a. This result agrees with Brechner et al. (2023) who observed a mode of ice crystals next to 200 μm typically occurring in updraft zones. While vapor

diffusion contributes to ice crystals in this size range, as proposed by Brechner et al. (2023), other mechanisms may also be involved. Indeed, our results in Fig. 4b suggest that this mode could also be a consequence of the BRK process.

To complete our analysis of the role of SIP processes in cloud top height decrease (see Section 3.2), it is important to highlight additional reasons for this change. One of them may arise from the depletion of cloud droplets caused by the presence of small ice crystals generated by SIP (as illustrated by drop evaporation in Fig. 8). This depletion could inhibit ice formation at upper levels (e.g., in the anvil) and may result in the production of a smaller amount of ice, consequently lowering the cloud top altitude.

Several other studies have also investigated the influence of SIP on cloud top altitude, other studies have investigated and reported further changes. Young et al. (2019) and Waman et al. (2022) found a decrease in cloud cover due to SIP (HM, DS, BRK and fragmentation during sublimation of ice crystals) which changes the amount of shortwave and longwave radiation. Conversely, the study of Qu et al. (2022) shows a larger cloud anvil when including DS process. Waman et al. (2022) also reported that lifetime decreases with SIP due to more rapid glaciation while Qu et al. (2022) found that DS extend the longevity of the cloud system. From our results, we did not detect any notable changes in the evolution of ice water content (IWC) or vertical wind speed that could indicate a shorter or longer lifetime due to SIP mechanisms. Additionally, introducing SIP processes into DESCAM does not significantly change the cloud cover. Although, it is important to remind that our simulations are based on a single cloud in an idealized framework, which could differ from larger, less constrained cloud systems.

The reduction of rainfall due to SIP and especially BRK depicted in Table. 2 has also been reported for a convective system in Hoarau et al. (2018) as well as in Han et al. (2024) who found

20% decrease in surface precipitation. However, the influence of SIP processes on precipitation remains uncertain: Dedekind et al. (2021) observed a reduction of precipitation in winter alpine mixed-phase cloud while Georgakaki et al. (2022) reported an increase of 30% for the same cloud type. As emphasized in Han et al. (2024), the effect of SIP on precipitation might depend on cloud type. Consequently, investigations about the impacts of SIP on drop size distribution, rainfall amount and evolution should be conducted in more details in a future work dedicated to a different cloud case.

5. Conclusions

In this study, we investigated the formation of ice crystals by secondary ice production (SIP) in an idealized deep convective cloud observed during the HAIC/HIWC campaign employing the 3D bin microphysics scheme DESCAM. Our analysis focuses on examining the temporal and spatial production rate of ice crystals by primary and secondary ice mechanisms, alongside their effects on particle size distribution. Secondly, the implications of implementing SIP processes (Hallett-Mossop, drop shattering and ice-ice breakup) in DESCAM are analyzed by looking at the cloud top altitude, vertical wind speed, latent heat release, relative humidity and precipitation amount.

Our results show that the first ice crystals to appear are generated by heterogeneous ice nucleation next to -7°C . After that, drops start to freeze causing the drop shattering (DS) process to dominate the production of ice crystals for a few minutes. However, both of these processes become rapidly insignificant because of cloud glaciation and the strong efficiency of Hallett-Mossop (HM) and ice-ice breakup (BRK) processes which become active with the presence of large ice crystals. Throughout the simulation, these two processes persist and become

the primary contributors to ice crystal formation below -30°C . Consequently, these two processes result in a simulated ice crystal number concentration close to those measured by in situ measurements during the HAIC/HIWC campaign for the mature stage of the cloud (the companion paper, Grzegorzczak et al., 2024).

Homogeneous and heterogeneous ice nucleation are the dominant mechanisms for ice crystal production in the anvil at temperatures below -30°C when air conditions become highly supersaturated ($\text{RH}_{\text{ice}} > 110\%$). Consequently, these processes are active during the formation stage of the cloud but cease to generate ice crystals once the cloud reaches its mature stage.

By examining particle size distributions along two trajectories using DESCAM bin microphysics scheme, we determined the conditions under which SIP and primary ice production (PIP) mechanisms occur, as well as their impact on particle size distributions (PSDs). Our results show that DS, HM, and PIP mechanisms produce small ice particles within 10-20 μm size range that can grow rapidly by vapor deposition. This potentially allows them to be identified in observational studies by using the method proposed by Korolev et al. (2020b).

As BRK process generates fragments which are similar in size to preexisting ice crystals, it does not lead to the emergence of a second mode of small ice crystals in PSDs, potentially complicating its detection in observational studies. Nevertheless, our results show that the presence of large ice particles coupled with high crystal concentrations is a marker of the BRK process. Therefore, this could also serve as an indicator for the occurrence of this process, particularly in situations where the supercooled liquid water content is low.

During the development phase of the cloud, the prolific generation of ice crystals by SIP processes results an intensified depletion of water vapor and an increase in latent heat release below 11 km altitude within the cloud system. This enhances convection below 11 km while

reducing it above (compared to a scenario without SIP processes) and leads to lowering the cloud top altitude by approximately 1.5 km.

When the cloud reaches its mature stage, sublimation is also enhanced by the numerous ice crystals generated by SIP mechanisms, leading to a narrower distribution of relative humidity compared to the simulation without SIP. As sublimation consumes latent heat, this could explain the presence of higher occurrence of downdrafts.

Our findings reveal that SIP processes lead to a reduction of the total amount of precipitation by around 15% as well as a reduction of the intense precipitation amount (> 40 mm) by 25%. A potential for future study could be addressed with a focus on the impacts of SIP on the liquid phase by simulating larger precipitating cloud systems such as the one studied with DESCAM model in Kagkara et al. (2020).

It should be noted that the conclusions of this study (Parts I and II) are specific to deep convective clouds. Future work should evaluate PIP and SIP as well as their impact on other cloud types, such as stratiform or orographic clouds. Furthermore, the implementation of SIP mechanisms in numerical models is a relatively recent and currently lacks reliability due to limited quantification of their efficiency. Additional studies are essential to better quantify SIP mechanisms and improve the reliability of these parameterizations in numerical models.

Acknowledgements

This work is part of the ACME project funded by the Agence Nationale de la Recherche (ANR) under the JCJC program, reference ANR-21-CE01-0003. The contribution from the lead author has been founded by the ACME project. This work was granted access to the HPC resources of [CINES/IDRIS/TGCC] under the allocations A0100105056 and A0160115061 made

by GENCI. We thank the team from HAIC/HIWC program for their contribution to data collection and sharing on the AERIS database. We acknowledge Alexei Korolev, Luis Ladino, Climate Change Canada (ECCC) and National Research Council (NRC) for sharing the UHSAS datasets.

Journal Pre-proof

References

- Billault-Roux, A.C., Georgakaki, P., Gehring, J., Jaffeux, L., Schwarzenboeck, A., Coutris, P., Nenes, A., Berne, A., 2023. Distinct secondary ice production processes observed in radar doppler spectra: insights from a case study. *Atmospheric Chemistry and Physics* 23, 10207–10234. URL: <https://acp.copernicus.org/articles/23/10207/2023/>, doi: 10.5194/acp-23-10207-2023.
- Brechner, P., McFarquhar, G.M., Schwarzenboeck, A., Korolev, A.V., 2023. Ice crystal size distributions in tropical mesoscale convective systems in the vicinity of darwin, australia: Results from the HAIC/HIWC campaign. *Journal of the Atmospheric Sciences* 80, 2147–2164. URL: <https://doi.org/10.1175/jas-d-22-0209.1>, doi: 10.1175/jas-d-22-0209.1.
- Choullarton, T., Latham, J., Mason, B.J., 1978. A possible mechanism of ice splinter production during riming. *Nature* 274, 791–792.
- Choullarton, T.W., Griggs, D.J., Humood, B.Y., Latham, J., 1980. Laboratory studies of riming, and its relation to ice splinter production. *Quarterly Journal of the Royal Meteorological Society* 106, 367–374. URL: <https://doi.org/10.1002/qj.49710644809>, doi: 10.1002/qj.49710644809.
- Clark, T., Hall, W., Coen, J., 1996. Source Code Documentation for the Clark-Hall Cloud-scale Model Code Version G3CH01. Technical Report. URL: <http://opensky.ucar.edu/islandora/object/technotes:193>, doi: 10.5065/D67W694V.
- Clark, T.L., 2003. Block-iterative method of solving the nonhydrostatic pressure in

- terrain-following coordinates: Two-level pressure and truncation error analysis. *Journal of Applied Meteorology* 42, 970–983. URL:
[http://dx.doi.org/10.1175/1520-0450\(2003\)042<0970:BMOSTN>2.0.CO;2](http://dx.doi.org/10.1175/1520-0450(2003)042<0970:BMOSTN>2.0.CO;2), doi: 10.1175/1520-0450(2003)042<0970:bmostn>2.0.co;2.
- Dedekind, Z., Lauber, A., Ferrachat, S., Lohmann, U., 2021. Sensitivity of precipitation formation to secondary ice production in winter orographic mixed-phase clouds. *Atmospheric Chemistry and Physics* 21, 15115–15134. URL:
<https://acp.copernicus.org/articles/21/15115/2021/>, doi: 10.5194/acp-21-15115-2021.
- Farrington, R.J., Connolly, P.J., Lloyd, G., Bower, K.N., Flynn, M.J., Gallagher, M.W., Field, P.R., Dearden, C., Choulaton, T.W., 2016. Comparing model and measured ice crystal concentrations in orographic clouds during the INUPIAQ campaign. *Atmospheric Chemistry and Physics* 16, 4945–4966. URL:
<https://doi.org/10.5194/acp-16-4945-2016>, doi: 10.5194/acp-16-4945-2016.
- Field, P.R., Lawson, R.P., Brown, P.R.A., Lloyd, G., Westbrook, C., Moisseev, D., Miltenberger, A., Nenes, A., Blyth, A., Choulaton, T., Connolly, P., Buehl, J., Crosier, J., Cui, Z., Dearden, C., DeMott, P., Flossmann, A., Heymsfield, A., Huang, Y., Kalesse, H., Kanji, Z.A., Korolev, A., Kirchgaessner, A., Lasher-Trapp, S., Leisner, T., McFarquhar, G., Phillips, V., Stith, J., Sullivan, S., 2017. Chapter 7. secondary ice production - current state of the science and recommendations for the future. *Meteorological Monographs* doi: 10.1175/amsmonographs-d-16-0014.1.
- Flossmann, A.I., Wobrock, W., 2010. A review of our understanding of the aerosol–cloud

interaction from the perspective of a bin resolved cloud scale modelling. *Atmospheric Research* 97, 478–497. URL:

<https://www.sciencedirect.com/science/article/pii/S0169809510001249>, doi: <https://doi.org/10.1016/j.atmosres.2010.05.008>. from the Lab to Models and Global Observations: Hans R. Pruppacher and Cloud Physics.

Fontaine, E., Schwarzenboeck, A., Leroy, D., Delanoë, J., Protat, A., Dezitter, F., Strapp, J.W., Lilie, L.E., 2020. Statistical analysis of ice microphysical properties in tropical mesoscale convective systems derived from cloud radar and in situ microphysical observations.

Atmospheric Chemistry and Physics 20, 3503–3553. URL:

<http://dx.doi.org/10.5194/acp-20-3503-2020>, doi: 10.5194/acp-20-3503-2020.

Fu, S., Deng, X., Shupe, M.D., Xue, H., 2019. A modelling study of the continuous ice formation in an autumnal arctic mixed-phase cloud case. *Atmospheric Research* 228, 77–85. URL:

<https://doi.org/10.1016/j.atmosres.2019.05.021>, doi: 10.1016/j.atmosres.2019.05.021.

Georgakaki, P., Sotiropoulou, G., Vignon, E., Billault-Roux, A.C., Berne, A., Nenes, A., 2022. Secondary ice production processes in wintertime alpine mixed-phase clouds.

Atmospheric Chemistry and Physics 22, 1965–1988. URL:

<https://acp.copernicus.org/articles/22/1965/2022/>, doi: 10.5194/acp-22-1965-2022.

Grzegorzczuk, P., Wobrock, W., Canzi, A., Niquet, L., Tridon, F., Planche, C., 2024. Investigating secondary ice production in a deep convective cloud with a 3d bin microphysics model:

Part i - sensitivity study of microphysical processes representations. Submitted to

Atmospheric Research.

Grzegorzcyk, P., Yadav, S., Zanger, F., Theis, A., Mitra, S.K., Borrmann, S., Szakáll, M., 2023.

Fragmentation of ice particles: laboratory experiments on graupel–graupel and graupel–snowflake collisions. *Atmospheric Chemistry and Physics* 23, 13505–13521.

URL: <https://acp.copernicus.org/articles/23/13505/2023/>, doi: 10.5194/acp-23-13505-2023.

Hallett, J., Mossop, S.C., 1974. Production of secondary ice particles during the riming process.

Nature 249, 26–28. URL: <https://doi.org/10.1038/249026a0>, doi: 10.1038/249026a0.

Han, C., Hoose, C., Dürlich, V., 2024. Secondary ice production in simulated deep convective clouds: A sensitivity study. *Journal of the Atmospheric Sciences* 81, 903–921. URL:

<http://dx.doi.org/10.1175/JAS-D-23-0156.1>, doi: 10.1175/jas-d-23-0156.1.

Heymsfield, A., Willis, P., 2014. Cloud conditions favoring secondary ice particle production in tropical maritime convection. *Journal of the Atmospheric Sciences* 71, 4500–4526. URL:

<http://dx.doi.org/10.1175/JAS-D-14-0093.1>, doi: 10.1175/jas-d-14-0093.1.

Heymsfield, A.J., Mossop, S.C., 1984. Temperature dependence of secondary ice crystal production during soft hail growth by riming. *Quarterly Journal of the Royal*

Meteorological Society 110, 765–770. URL:

<http://dx.doi.org/10.1002/qj.49711046512>, doi: 10.1002/qj.49711046512.

Hiron, T., Flossmann, A., 2015. A study of the role of the parameterization of heterogeneous ice

nucleation for the modeling of microphysics and precipitation of a convective cloud.

Journal of the Atmospheric Sciences 72, 3322–3339.

Hoarau, T., Pinty, J.P., Barthe, C., 2018. A representation of the collisional ice break-up process in the two-moment microphysics lima v1.0 scheme of meso-nh. Geoscientific Model Development 11, 4269–4289. URL:

<https://gmd.copernicus.org/articles/11/4269/2018/>, doi: 10.5194/gmd-11-4269-2018.

Hu, Y., McFarquhar, G.M., Wu, W., Huang, Y., Schwarzenboeck, A., Protat, A., Korolev, A., Rauber, R.M., Wang, H., 2021. Dependence of ice microphysical properties on environmental parameters: Results from haic-hiwc cayenne field campaign. Journal of the Atmospheric Sciences URL:

<http://dx.doi.org/10.1175/JAS-D-21-0015.1>, doi: 10.1175/jas-d-21-0015.1.

Huang, Y., Wu, W., McFarquhar, G.M., Xue, M., Morrison, H., Milbrandt, J., Korolev, A.V., Hu, Y., Qu, Z., Wolde, M., Nguyen, C., Schwarzenboeck, A., Heckman, I., 2022. Microphysical processes producing high ice water contents (hiwcs) in tropical convective clouds during the haic-hiwc field campaign: dominant role of secondary ice production.

Atmospheric Chemistry and Physics 22, 2365–2384. URL:

<https://acp.copernicus.org/articles/22/2365/2022/>, doi: 10.5194/acp-22-2365-2022.

James, R.L., Crosier, J., Connolly, P.J., 2023. A bin microphysics parcel model investigation of secondary ice formation in an idealised shallow convective cloud. Atmospheric Chemistry and Physics 23, 9099–9121. URL:

<http://dx.doi.org/10.5194/acp-23-9099-2023>, doi:

10.5194/acp-23-9099-2023.

Järvinen, E., McCluskey, C.S., Waitz, F., Schnaiter, M., Bansemer, A., Bardeen, C.G., Gettelman, A., Heymsfield, A., Stith, J.L., Wu, W., D'Alessandro, J.J., McFarquhar, G.M., Diao, M., Finlon, J.A., Hill, T.C.J., Levin, E.J.T., Moore, K.A., DeMott, P.J., 2022. Evidence for secondary ice production in southern ocean maritime boundary layer clouds. *Journal of Geophysical Research: Atmospheres* 127. URL:

<http://dx.doi.org/10.1029/2021JD036411>, doi: 10.1029/2021jd036411.

Kagkara, C., Wobrock, W., Planche, C., Flossmann, A.I., 2020. The sensitivity of intense rainfall to aerosol particle loading – a comparison of bin-resolved microphysics modelling with observations of heavy precipitation from hymex iop7a. *Natural Hazards and Earth System Sciences* 20, 1469–1483. URL:

<http://dx.doi.org/10.5194/nhess-20-1469-2020>, doi:

10.5194/nhess-20-1469-2020.

Karalis, M., Sotiropoulou, G., Abel, S.J., Bossioli, E., Georgakaki, P., Methymaki, G., Nenes, A., Tombrou, M., 2022. Effects of secondary ice processes on a stratocumulus to cumulus transition during a cold-air outbreak. *Atmospheric Research* 277, 106302. URL:

<http://dx.doi.org/10.1016/j.atmosres.2022.106302>, doi:

10.1016/j.atmosres.2022.106302.

Keinert, A., Spannagel, D., Leisner, T., Kiselev, A., 2020. Secondary ice production upon freezing of freely falling drizzle droplets. *Journal of the Atmospheric Sciences* 77, 2959–2967.

URL: <https://doi.org/10.1175/jas-d-20-0081.1>, doi:

10.1175/jas-d-20-0081.1.

- Koop, T., Luo, B., Tsias, A., Peter, T., 2000. Water activity as the determinant for homogeneous ice nucleation in aqueous solutions. *Nature* 406, 611–614. URL: <http://dx.doi.org/10.1038/35020537>, doi: 10.1038/35020537.
- Korolev, A., DeMott, P.J., Heckman, I., Wolde, M., Williams, E., Smalley, D.J., Donovan, M.F., 2022. Observation of secondary ice production in clouds at low temperatures. *Atmospheric Chemistry and Physics* 22, 13103–13113. URL: <https://acp.copernicus.org/articles/22/13103/2022/>, doi: 10.5194/acp-22-13103-2022.
- Korolev, A., Heckman, I., Wolde, M., Ackerman, A.S., Fridlind, A.M., Ladino, L.A., Lawson, R.P., Milbrandt, J., Williams, E., 2020 a. A new look at the environmental conditions favorable to secondary ice production. *Atmospheric Chemistry and Physics* 20, 1391–1429. URL: <http://dx.doi.org/10.5194/acp-20-1391-2020>, doi: 10.5194/acp-20-1391-2020.
- Korolev, A., Heckman, I., Wolde, M., Ackerman, A.S., Fridlind, A.M., Ladino, L.A., Lawson, R.P., Milbrandt, J., Williams, E., 2020 b. A new look at the environmental conditions favorable to secondary ice production. *Atmospheric Chemistry and Physics* 20, 1391–1429. URL: <http://dx.doi.org/10.5194/acp-20-1391-2020>, doi: 10.5194/acp-20-1391-2020.
- Korolev, A., Leisner, T., 2020. Review of experimental studies of secondary ice production. *Atmospheric Chemistry and Physics* 20, 11767–11797. doi: 10.5194/acp-20-11767-2020.
- Ladino, L.A., Korolev, A., Heckman, I., Wolde, M., Fridlind, A.M., Ackerman, A.S., 2017. On the role of ice-nucleating aerosol in the formation of ice particles in tropical mesoscale convective systems. *Geophysical Research Letters* 44, 1574–1582. URL:

<https://agupubs.onlinelibrary.wiley.com/doi/abs/10.1002/2016GL072455>, doi: <https://doi.org/10.1002/2016GL072455>,
arXiv:<https://agupubs.onlinelibrary.wiley.com/doi/pdf/10.1002/2016GL072455>.

Lasher-Trapp, S., Kumar, S., Moser, D.H., Blyth, A.M., French, J.R., Jackson, R.C., Leon, D.C., Plummer, D.M., 2018. On different microphysical pathways to convective rainfall. *Journal of Applied Meteorology and Climatology* 57, 2399–2417. URL: <https://doi.org/10.1175/jamc-d-18-0041.1>, doi: 10.1175/jamc-d-18-0041.1.

Lauber, A., Kiselev, A., Pander, T., Handmann, P., Leisner, T., 2018. Secondary ice formation during freezing of levitated droplets. *Journal of the Atmospheric Sciences* 75, 2815–2826. URL: <https://doi.org/10.1175/jas-d-18-0052.1>, doi: 10.1175/jas-d-18-0052.1.

Lawson, R.P., Korolev, A.V., DeMott, P.J., Heymsfield, A.J., Brientjes, R.T., Wolff, C.A., Woods, S., Patnaude, R.J., Jensen, J.B., Moore, K.A., Heckman, I., Rosky, E., Haggerty, J., Perkins, R.J., Fisher, T., Hill, T.C.J., 2023. The secondary production of ice in cumulus experiment (spicule). *Bulletin of the American Meteorological Society* 104, E51–E76. URL: <http://dx.doi.org/10.1175/BAMS-D-21-0209.1>, doi: 10.1175/bams-d-21-0209.1.

Lawson, R.P., Woods, S., Morrison, H., 2015. The microphysics of ice and precipitation development in tropical cumulus clouds. *Journal of the Atmospheric Sciences* 72, 2429–2445. URL: <https://doi.org/10.1175/jas-d-14-0274.1>, doi: 10.1175/jas-d-14-0274.1.

- Leroy, D., Monier, M., Wobrock, W., Flossmann, A.I., 2006. A numerical study of the effects of the aerosol particle spectrum on the development of the ice phase and precipitation formation. *Atmospheric Research* 80, 15–45. URL: <http://dx.doi.org/10.1016/j.atmosres.2005.06.007>, doi: 10.1016/j.atmosres.2005.06.007.
- Leroy, D., Wobrock, W., Flossmann, A.I., 2009. The role of boundary layer aerosol particles for the development of deep convective clouds: A high-resolution 3d model with detailed (bin) microphysics applied to crystal-face. *Atmospheric Research* 91, 62–78. URL: <http://dx.doi.org/10.1016/j.atmosres.2008.06.001>, doi: 10.1016/j.atmosres.2008.06.001.
- Monier, M., Wobrock, W., Gayet, J.F., Flossmann, A., 2006. Development of a detailed microphysics cirrus model tracking aerosol particles' histories for interpretation of the recent inca campaign. *Journal of the Atmospheric Sciences* 63, 504–525. URL: <http://dx.doi.org/10.1175/JAS3656.1>, doi: 10.1175/jas3656.1.
- Morrison, H., Milbrandt, J.A., 2015. Parameterization of cloud microphysics based on the prediction of bulk ice particle properties. part i: Scheme description and idealized tests. *Journal of the Atmospheric Sciences* 72, 287 – 311. URL: <https://journals.ametsoc.org/view/journals/atms/72/1/jas-d-14-0065.1.xml>, doi: 10.1175/JAS-D-14-0065.1.
- Mossop, S.C., 1976. Production of secondary ice particles during the growth of graupel by riming. *Quarterly Journal of the Royal Meteorological Society* 102, 45–57. URL: <https://doi.org/10.1002/qj.49710243104>, doi: 10.1002/qj.49710243104.
- Niquet, L., Tridon, F., Grzegorzczak, P., Causse, A., Bordet, B., Wobrock, W., Planche, C., 2024.

- Evaluation of the representation of raindrop self-collection and breakup in two-moment bulk models using a multifrequency radar retrieval. *Journal of Geophysical Research: Atmospheres* 129. URL: <http://dx.doi.org/10.1029/2024JD041269>, doi: 10.1029/2024jd041269.
- Phillips, V.T.J., Patade, S., Gutierrez, J., Bansemer, A., 2018. Secondary ice production by fragmentation of freezing drops: Formulation and theory. *Journal of the Atmospheric Sciences* 75, 3031–3070. URL: <https://doi.org/10.1175/jas-d-17-0190.1>, doi: 10.1175/jas-d-17-0190.1.
- Phillips, V.T.J., Yano, J.I., Khain, A., 2017. Ice Multiplication by Breakup in Ice–Ice Collisions. Part I: Theoretical Formulation. *Journal of the Atmospheric Sciences* 74, 1705–1719. doi: 10.1175/JAS-D-16-0224.1.
- Planche, C., Tridon, F., Banson, S., Thompson, G., Monier, M., Battaglia, A., Wobrock, W., 2019. On the realism of the rain microphysics representation of a squall line in the wrf model. part ii: Sensitivity studies on the rain drop size distributions. *Monthly Weather Review* 147, 2811–2825. URL: <http://dx.doi.org/10.1175/MWR-D-18-0019.1>, doi: 10.1175/mwr-d-18-0019.1.
- Planche, C., Wobrock, W., Flossmann, A.I., Tridon, F., Van Baelen, J., Pointin, Y., Hagen, M., 2010. The influence of aerosol particle number and hygroscopicity on the evolution of convective cloud systems and their precipitation: A numerical study based on the cops observations on 12 august 2007. *Atmospheric Research* 98, 40–56. URL: <http://dx.doi.org/10.1016/j.atmosres.2010.05.003>, doi: 10.1016/j.atmosres.2010.05.003.
- Qu, Y., Khain, A., Phillips, V., Ilotoviz, E., Shpund, J., Patade, S., Chen, B., 2020. The role of ice

- splintering on microphysics of deep convective clouds forming under different aerosol conditions: Simulations using the model with spectral bin microphysics. *Journal of Geophysical Research: Atmospheres* 125. URL: <http://dx.doi.org/10.1029/2019JD031312>, doi: 10.1029/2019jd031312.
- Qu, Z., Korolev, A., Milbrandt, J.A., Heckman, I., Huang, Y., McFarquhar, G.M., Morrison, H., Wolde, M., Nguyen, C., 2022. The impacts of secondary ice production on microphysics and dynamics in tropical convection. *Atmospheric Chemistry and Physics* 22, 12287–12310. URL: <http://dx.doi.org/10.5194/acp-22-12287-2022>, doi: 10.5194/acp-22-12287-2022.
- Sotiropoulou, G., Ickes, L., Nenes, A., Ekman, A.M.L., 2021. Ice multiplication from ice–ice collisions in the high arctic: sensitivity to ice habit, rimed fraction, ice type and uncertainties in the numerical description of the process. *Atmospheric Chemistry and Physics* 21, 9741–9760. URL: <http://dx.doi.org/10.5194/acp-21-9741-2021>, doi: 10.5194/acp-21-9741-2021.
- Takahashi, T., Nagao, Y., Kushiyama, Y., 1995. Possible high ice particle production during graupel–graupel collisions. *Journal of the Atmospheric Sciences* 52, 4523–4527. doi: 10.1175/1520-0469(1995)052<4523:phippd>2.0.co;2.
- von Terzi, L., Neto, J.D., Ori, D., Myagkov, A., Kneifel, S., 2022. Ice microphysical processes in the dendritic growth layer: a statistical analysis combining multi-frequency and polarimetric doppler cloud radar observations. *Atmospheric Chemistry and Physics* 22, 11795–11821. URL: <https://doi.org/10.5194/acp-22-11795-2022>, doi: 10.5194/acp-22-11795-2022.

Tridon, F., Planche, C., Mroz, K., Banson, S., Battaglia, A., Van Baelen, J., Wobrock, W., 2019.

On the realism of the rain microphysics representation of a squall line in the wrf model.

part i: Evaluation with multifrequency cloud radar doppler spectra observations. *Monthly*

Weather Review 147, 2787–2810. URL:

<http://dx.doi.org/10.1175/MWR-D-18-0018.1>, doi:

10.1175/mwr-d-18-0018.1.

Vardiman, L., 1978. The generation of secondary ice particles in clouds by crystal–crystal

collision. *Journal of the Atmospheric Sciences* 35, 2168–2180. URL:

[https://doi.org/10.1175/1520-0469\(1978\)035<2168:tgosip>2.0.](https://doi.org/10.1175/1520-0469(1978)035<2168:tgosip>2.0.co;2)

[co;2](https://doi.org/10.1175/1520-0469(1978)035<2168:tgosip>2.0.co;2), doi: 10.1175/1520-0469(1978)035<2168:tgosip>2.0.co;2.

Waman, D., Patade, S., Jadav, A., Deshmukh, A., Gupta, A.K., Phillips, V.T.J., Bansemmer, A.,

DeMott, P.J., 2022. Dependencies of four mechanisms of secondary ice production on

cloud-top temperature in a continental convective storm. *Journal of the Atmospheric*

Sciences 79, 3375–3404. URL:

<https://doi.org/10.1175/jas-d-21-0278.1>, doi: 10.1175/jas-d-21-0278.1.

Young, G., Lachlan-Cope, T., O’Shea, S.J., Dearden, C., Listowski, C., Bower, K.N., Choularton,

T.W., Gallagher, M.W., 2019. Radiative effects of secondary ice enhancement in coastal

antarctic clouds. *Geophysical Research Letters* 46, 2312–2321. URL:

<http://dx.doi.org/10.1029/2018GL080551>, doi: 10.1029/2018gl080551.

Zhao, X., Liu, X., 2021. Global importance of secondary ice production. *Geophysical Research*

Letters 48. URL: <http://dx.doi.org/10.1029/2021GL092581>, doi:

10.1029/2021gl092581.

Zhao, X., Liu, X., 2022. Primary and secondary ice production: interactions and their relative

importance. Atmospheric Chemistry and Physics 22, 2585–2600. URL:

<http://dx.doi.org/10.5194/acp-22-2585-2022>, doi:

10.5194/acp-22-2585-2022.

Journal Pre-proof

Pierre Grzegorzczuk: Writing – review & editing, Writing – original draft, Visualization, Validation, Methodology, Investigation, Software, Formal analysis.

Wolfram Wobrock: Writing – review & editing, Writing – original draft, Software, Supervision, Validation, Methodology, Investigation, Conceptualization.

Antoine Canzi: Writing – original draft, Validation, Software, Formal analysis

Laurence Niquet: Writing – original draft, Validation

Frédéric Tridon: Writing – original draft, Validation

Céline Planche: Writing – review & editing, Writing – original draft, Conceptualization, Resources, Supervision, Project administration, Funding acquisition, Validation, Methodology, Investigation.

Journal Pre-proof

Declaration of interests

- The authors declare that they have no known competing financial interests or personal relationships that could have appeared to influence the work reported in this paper.
- The author is an Editorial Board Member/Editor-in-Chief/Associate Editor/Guest Editor for *[Journal name]* and was not involved in the editorial review or the decision to publish this article.
- The authors declare the following financial interests/personal relationships which may be considered as potential competing interests:

Journal Pre-proof